J Mater Sci (2009) 44:1264–1274
DOI 10.1007/s10853-008-3241-6

Study the sintering behavior of nanocrystalline 3Y-TZP/430L stainless-steel composite layers for co-powder injection molding

M. Dourandish · A. Simchi

Received: 17 September 2008 / Accepted: 31 December 2008 /

Abstract Recently, co-powder injection molding process (2C-PIM) has attained considerable interest to fabricate complex-shaped functional materials. The aim of this work is to study the sintering compatibility between nanocrystalline yttria-stabilized zirconia (3Y-TZP) and PIM grade 430L stainless steel (SS) powders, which is the utmost important step in the 2C-PIM process. To evaluate the mismatch strain development during the co-sintering, the isothermal and nonisothermal behaviors of the ceramic and metal powders were studied. Small bilayers of 3Y-TZP/430L were made by a powder metallurgy technique and the feasibility of simultaneous sintering and joining of the composite layer was examined. Electron probe micro-analyzer (EPMA) was used to study the joint interface. The shear strength of the bond was tested by a shear-punch instrument. It is shown that the amount of mismatch sintering shrinkage between the zirconia ceramic and SS powder during sintering can be as high as 9.7%. Meanwhile, sintering in vacuum induced lower mismatch strain compared to argon sintering. It is also shown that formation of a liquid phase by boron addition to the SS layer could assist bonding. The liquid phase accommodates the mismatch sintering shrinkage and ease materials transfer at the interface. EPMA analysis confirmed the interlayer diffusion of Zr, Fe, and Cr during sintering to form a ternary Zr–Fe–Cr oxide interface.

M. Dourandish · A. Simchi
Department of Materials Science and Engineering, Sharif University of Technology, P.O. Box 11365-9466, 14588 Tehran, Iran

A. Simchi (✉)
Institute for Nanoscience and Nanotechnology (INST), Sharif University of Technology, P.O. Box 11365-9466, 14588 Tehran, Iran
e-mail: simchi@sharif.edu

Introduction

Due to the superior properties of zirconia ceramics such as fracture toughness, strength, wear resistance, and oxide conductivity, the materials have extensively been used in structure and electrical applications [1–3]. To further improve the functionality and cost reduction in engineering applications, for example in the gas turbines, engines, and solid oxide fuel cells, fabrication of metal/ceramic composite parts by various joining methods have been studied frequently. So far, manufacturing of metal/ceramic joints, which can withstand high-temperature environments, has been the subject of interest for many years [4]. The most common existing techniques include adhesives bonding, solid-state bonding, and brazing [5–7]. In these methods, disadvantages of an extra manufacturing step and addition of a third (join-) material different from the ceramic and metal are imposed. So far, direct joining of dissimilar materials has investigated frequently. For instance, Weng et al. [8] have used tape casting process to produce nickel–zirconia multilayer for anode supported solid oxide fuel cells; Harach and Vecchio [9] have studied reactive joining of Al/Al_3Ti; Yeo et al. [10] have shown the feasibility of producing multilayer functionally graded zirconia/316L SS by tape casting; Biswas and Upadhyaya [11] have utilized slurry coating and sintering to produce a tungsten alloy layer on alumina substrate; Yun and Lombardo [12] have investigated the gas permeability of laminated green ceramic tapes; hot isostatic pressing of ceramics/Incoloy 909 composite structures has been studied by Larker et al.

[13]; multi-billet extrusion of multilayer 316L/PSZ gradient composite pipes has been performed by Zhang et al. [14]. Sinter-joining and diffusion-bonding of zirconia thin films to Co–Cr–Mo alloy [15], sialon ceramic to austenitic and ferritic stainless steels [16], copper to alumina [17], silicon carbide to a nickel base superalloy [18], vanadium to alumina [19], silicon nitride to carbon steel [20], zirconia to stainless steels [21], hydroxyapatite to zirconia [22], ZrO_2 to NiCr alloy [23], and Ni to YSZ [24] have also been examined. In essence, results of previous studies indicated that significant differences in the thermal and mechanical properties induce serious difficulties in direct joining of metals and ceramics [4].

Powder metallurgy is a near-net manufacturing procedure with great advantages for producing functionally graded components and composites with different properties in various locations [25]. So far, different sintering procedures such as current-activated sintering [26, 27], high pressure sintering [28], pressureless sintering [29], spark plasma sintering [30, 31], and reaction sintering [32] have been examined. Recently, the reward of powder injection molding (PIM) has attracted a great interest for fabrication of complex-shaped two-component parts [33]. The process, which is termed co-powder injection molding (2C-PIM) has been the subject of intensive research during the past few years [34]. Alcock et al. [35] have studied the co-injection molding process for 316L/carbonyle iron as a core/shell component. Heaney et al. [36] have investigated the sintering behavior of co-injection molded parts made from tool steel with stainless steel. Imgrund et al. [37, 38] and Ruh et al. [33] have used the process for fabrication of micro-sized parts. The present authors have recently reported the co-sintering behavior of 17-4PH/316L [38, 39], Inconel 718/Inconel 625 [40], M2/316L [41], and porosity-graded Co–Cr–Mo alloy [42]. Sintering studies on ZrO_2/Al_2O_3 [43], 3Y-TZP/stainless steel [44, 45], Al_2O_3/Ce-TZP [46], alumina/zirconia hybrid laminates [47, 48], glass/alumina [49], glass/ceramic-filled glass [50], and W/Al_2O_3 bilayers [51] have also been performed.

In light of the results reported so far, it can be highlighted that for successful manufacturing of composite layers, it is vital to minimize the mismatch shrinkage and shrinkage rate during the sintering process. In the present work, the sintering behavior of 3Y-TZP/430L SS stepwise graded composite layer was investigated. A pressureless sintering method combined with a simple powder layering technique was used to fabricate the ceramic/metal layer. Meanwhile, due to the high melting point of advanced ceramics and with the aim of decreasing the sintering temperature, nanocrystalline zirconia ceramic were utilized for the direct-joining. In order to improve wetting of the ceramic by metal and facilitate joining, liquid phase sintering in the presence of iron–boron melt was also examined. It is well documented that boron reacts with iron at sintering temperature to form a eutectic melt at ~1,170 °C [52]. The liquid contributes to densification via liquid phase sintering [53, 54]. The benefits of boron addition to stainless-steel sintering have frequently been reported, for example by Tonnes [55] and Suri et al. [56]. Here, it is worth noting that the experimental work performed in this paper is a simulated condition of the brown parts produced by the 2C-PIM process; hence, the mechanisms governing co-sintering in the work cannot be entirely applied to PIM green/de-bound parts as regard PIM involves addition of polymers (40–50 vol.%) that can affect the sintering behavior.

Experimental procedure

The starting materials used in the present work were yttria-stabilized zirconia powder (Tosoh, Japan) with an average particle size of 150 nm (Fig. 1a), 430L stainless steel powder (Sandvik Osprey, UK) with an average particle size of 10 μm (Fig. 1b), and a high purity amorphous boron powder (Aldrich, Germany) with particle size <1 μm. The characteristics of the ceramic and steel powders are

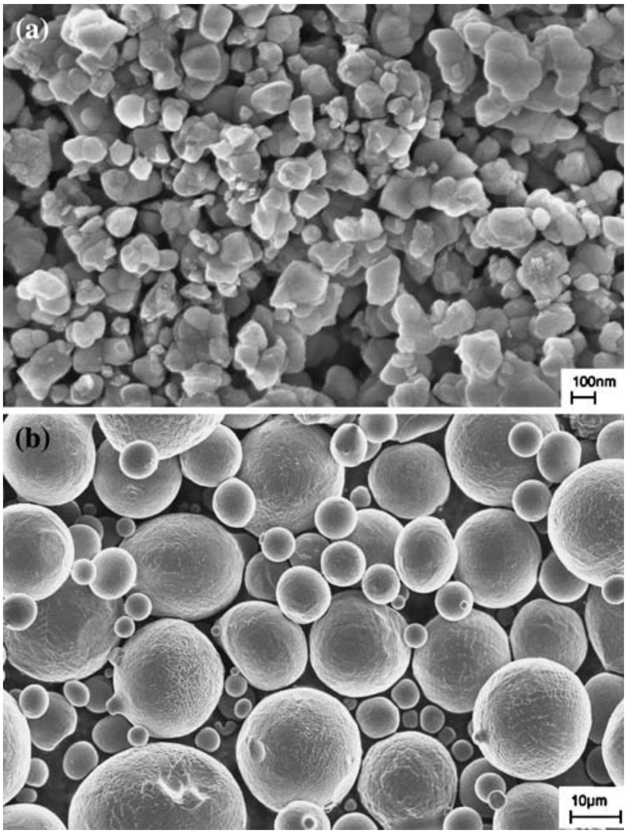

Fig. 1 SEM micrographs showing **a** 3Y-TZP and **b** 430L stainless steel powder particles

Table 1 Characteristics of powders used in this study

Powder	Designation	Nominal composition	Fractional apparent density	Fractional tap density	Angle of repose
Zirconia	3Y-TZP	$3Y_2O_3$ (mol.%)	0.18	0.29	54°
Stainless steel	430L SS	17Cr–0.09C–0.4Si–0.5Mn (wt%)	0.21	0.51	64°

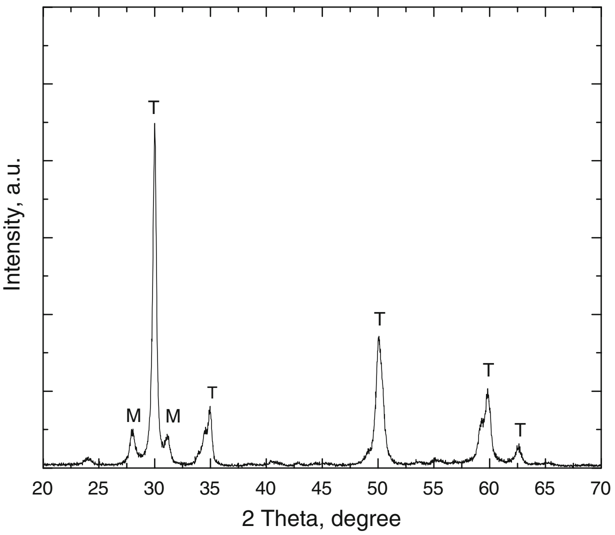

Fig. 2 X-ray diffraction pattern of nanocrystalline 3Y-TZP powder. *M* Monolithic, *T* Tetragonal

reported in Table 1. The X-ray diffraction pattern of the zirconia powder taken by Cu Kα radiation (Simens D5000, Germany) is shown in Fig. 2. The average crystallite size was determined by Scherrer equation [57] and found to be 27 nm. The weight fraction of the monoclinic phase was calculated using the Torayal equation [58] and found to be 22%.

As seen in Table 1, the tap density of the zirconia ceramic is significantly lower than that of the stainless steel, which induces significant mismatch shrinkage during co-sintering. To adjust the total shrinkage of the zirconia ceramic, the 3Y-TZP powder was compacted in a cylindrical steel die (7 mm diameter) at 150 MPa to obtain fractional density of ~0.5. The sintering behavior of the 3Y-TZP compact and SS powder was studied by a sinter dilatometer (TMA 801, Netzsch, Germany). The heating and cooling rates were 5 and 10 K min^{-1}, respectively. High purity argon (dew point <-60 °C) and vacuum ($\sim 10^{-2}$ mbar) atmospheres were examined. The sintering shrinkage and shrinkage rate versus temperature were recorded and the temperatures of sintering start (T_s) and maximum strain rate (T_{max}) were determined. The sintering response of the materials was also studied by employing a laboratory batch furnace running under the argon and vacuum atmospheres at 1,350 °C. The dwell time was 1, 120, and 240 min. The heating and cooling rates were 5 and 10 K min^{-1}, respectively.

In order to evaluate the sintering response of the composite layers, bilayers of 3Y-TZP with 430L and 430B (430L + 0.2wt% B) were made in an alumina tube coated with boron nitride. To prepare the 430B layer, the stainless steel powder was mixed with 0.2%B in a Turbula mixer (BASEL, Switzerland) for 20 min. The zirconia ceramic disk was inserted into the alumina tube and the 430L or 430B powder was poured into the tube. The die was slightly tapped to spread the powder evenly at its bottom. Light pressure (~40 kPa) was applied to flatten the layer. The bilayers were then sintered in the laboratory furnace as explained above. The water immersion (Archimedes') method (ISO Standard 5017; 1998) was used to determine the density of the sintered materials. For microstructural evaluation, the layers were cut in the direction of hand pressing and metallographic sections were prepared according to the common method of grinding on emery papers and polishing with diamond paste. Optical and high-resolution scanning electron microscopy (FEG-SEM, Gemini, Zeiss, Germany) were used for the microstructural study. A SX100 electron probe micro-analyzer (EPMA, Cameca, France) under an acceleration voltage of 25 kV and beam current of 20 nA was employed to investigate the diffusion of elements along the interface boundary during sintering.

Shear test is a common method to evaluate the strength of dissimilar joints [59]. In this work, shear-punch test was conducted. Figure 3 shows the punch-die assembly. Doughnut shape samples (OD: 10 mm, ID: 5 mm, *h*: 4 mm)

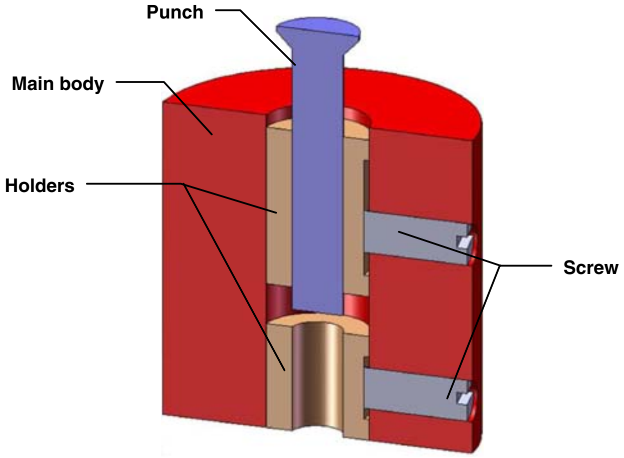

Fig. 3 Schematic drawing showing the shear-punch die assembly used for measuring of the bond strength

were prepared by die pressing of the zirconia ceramic at 150 MPa to attain fractional density of ~0.5. Then, the stainless steel powder (430L or 430B) was poured into the die and flattened by applying ~40 kPa pressure. The composite was then sintered in the laboratory furnace as explained above. The cylindrical sample was filled into the hole of the mold i.e., the interface area located at the cross-section of two parts of the clamp, which will be subjected to the tension load like a tensile test. Under this condition, the shear stress is applied to the interface area by pulling the two parts of the clamp. A shear force was applied by an Instron-6027 tensile test machine at the cross speed of 2 mm/min to determine the bond strength. Three samples were tested for each composite layer and the average was reported as the fracture strength.

Results

Figure 4 shows the nonisothermal sintering behavior of 3Y-TZP and 430L SS powders in argon and vacuum atmospheres. The comparative data of sintering response are reported in Table 2. In the 3Y-TZP compact sintered in argon atmosphere, shrinkage started at 1,131 °C and proceeded at the maximum rate at 1,287 °C. Under vacuum atmosphere, the start of shrinkage (0.5%) is nearly the same as argon (1,129 °C); however, the temperature of maximum shrinkage rate was higher than that of the sample sintered in argon. It appears that vacuum sintering decreased the sintering kinetics of the 3Y-TZP compact. Experimental results indicated faster sintering kinetics of 430L SS, i.e., the sintering starts at 907 °C (argon) and 939°C (vacuum). Considering the maximum shrinkage rate

Table 2 Dilatometry data of 3Y-TZP and 430L stainless steel powders

Material	Atmosphere	$T_{0.5}$ (°C)	T_{Max} (°C)	ε (%)
3Y-TZP	Argon	1131	1289	7.8
	Vacuum	1129	1319	12.6
430L SS	Argon	907	1223	10.4
	Vacuum	939	1024	3.5

$T_{0.5}$ Temperature at 0.5% shrinkage, T_{Max} temperature at maximum shrinkage rate, ε strain at T_{Max}

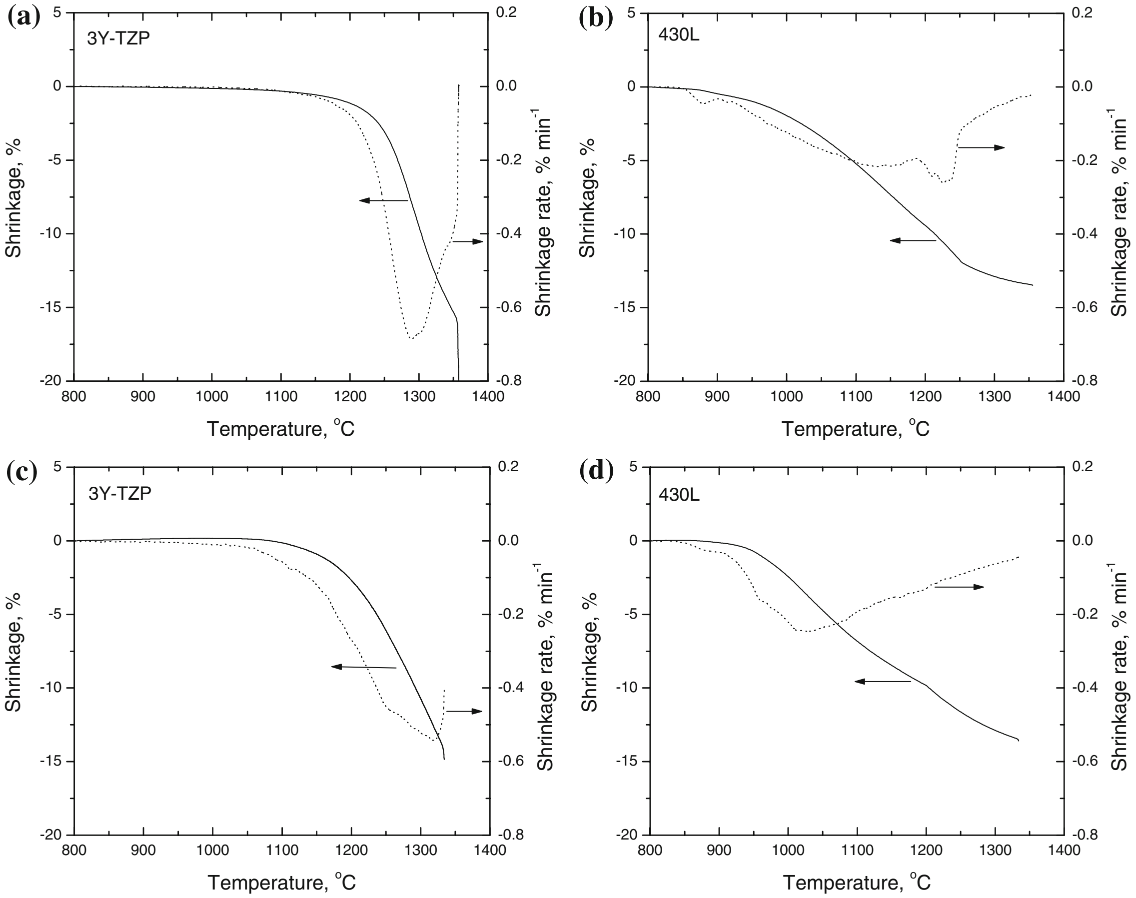

Fig. 4 Shrinkage and shrinkage rate of 3Y-TZP and 430L SS powders during nonisothermal sintering in argon (**a**, **b**) and vacuum (**c**, **d**) atmospheres

of the stainless steel powder, which occurred at 1,223 and 1,024 °C for the argon and vacuum sintering, respectively, the ceramic and metal counterparts should exhibit better compatibility during co-sintering in argon. It should be noted that the mismatch strain ($\Delta\varepsilon$) and mismatch strain rate ($\Delta\dot{\varepsilon}$) at the interface region could lead to warpage and cracking of the composite layer. Figure 5 shows the amount of $\Delta\varepsilon$ and $\Delta\dot{\varepsilon}$ as a function of time during non-isothermal and isothermal sintering cycles. As seen, the maximum mismatch strain during nonisothermal sintering is 7.5% at 1,161 °C for vacuum while it is 8.6% at 1,148 °C for argon. It was shown elsewhere [60] that total mismatch shrinkage over ±5% induces high stresses that can distort (deform) the layers. Here, plastic deformation of metals at the high temperature accommodates the mismatch stresses. In the case of ceramic-to-metal sintering, the amount of mismatch strain should be lower because the mismatch stresses at the interface cannot be completely accommodated by plastic deformation and cracking of the ceramic interface is likely to occur. Feng et al. [43] have conducted co-sintering of zirconia/alumina membranes with significant mismatch shrinkage, i.e., 8%. Ruh et al. [33] have reported mismatch shrinkage of ~5% during co-sintering of micro-sized co-injection molded Al_2O_3/ZrO_2 components. They have shown that the small contact area could accommodate the mismatch stress by distortion or edge-cracking (dependent on the amount of the stresses).

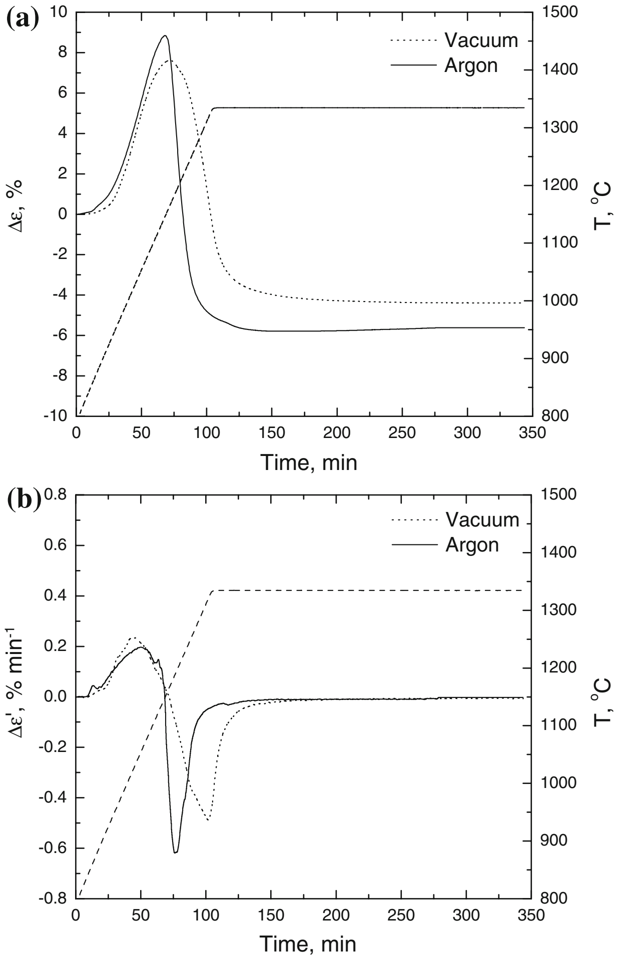

Fig. 5 **a** Mismatch strain ($\Delta\varepsilon$) and **b** mismatch strain rate ($\Delta\dot{\varepsilon}$) between 3Y-TZP and 430L SS powders sintered in argon and vacuum atmospheres. The temperature cycle is shown in the plot, exhibiting nonisothermal and isothermal sintering regions

In addition to the instantaneous shrinkage and shrinkage rate during sintering, the total shrinkage of the layers after completing the sintering process is important. Table 3 shows the results of batch sintering of the investigated materials at 1,350 °C for different times in argon and vacuum atmospheres. It is evident that for successful co-sintering, the total shrinkage of the layers should be as close as together; otherwise, cracking and delamination of the interface and/or distortion of the metallic part are feasible. Nevertheless, the difference between the linear shrinkage of the ceramic and stainless steel powders is about 2.6% in the case of argon sintering for 240 min (Table 3). Meanwhile, adjustment of the green density of the powders is required to prevent the total mismatch shrinkage. Although it is difficult to precisely adjust the green density of layers by the pressureless sintering procedure used in the present work, by controlling the amount of solids concentration of the PIM feedstocks, this aim can easily be attained.

Figure 6 shows micrographs taken from the interface zone of the ceramic/metal composite layer sintered at 1,350 °C for 240 min in argon. The optical micrograph (Fig. 6a) indicates partial bonding of the materials during the sintering process. The sharp interface indicates very

Table 3 Fractional density of isothermally sintered layers at 1,350 °C in argon and vacuum for different times

Material	Atmosphere	Dwell time (min)	Relative density	Radial shrinkage (%)
3Y-TZP	Ar	1	0.77	16.5
		120	0.87	18.2
		240	0.90	19.8
	Vac	1	–	–
		120	0.82	15.9
		240	0.84	17.2
430L SS	Ar	1	0.76	13.0
		120	0.94	16.1
		240	0.96	17.2
	Vac	1	–	–
		120	0.95	16.5
		240	0.96	17.4

– Not measured

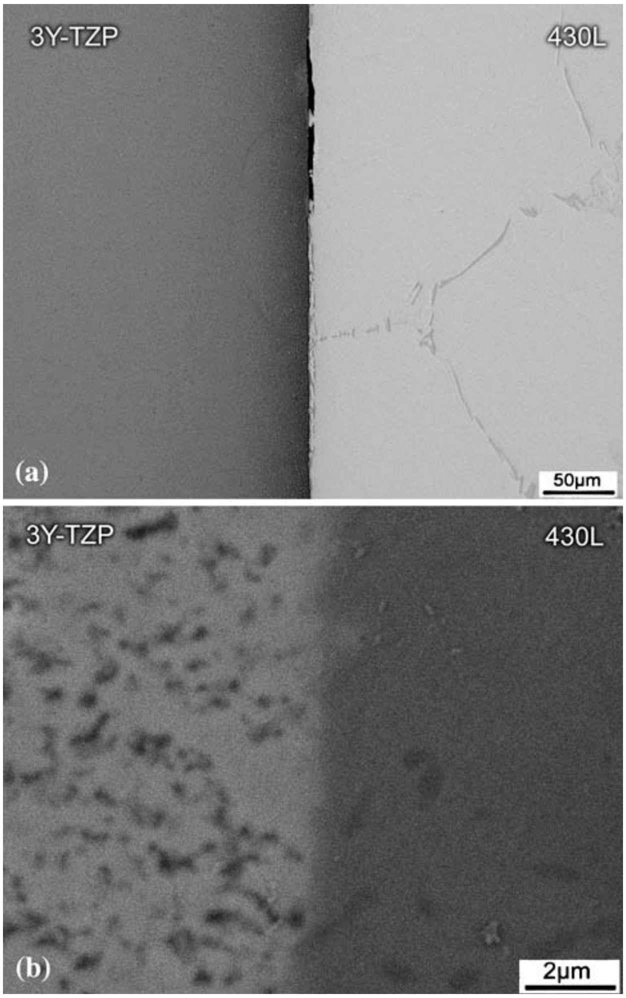

Fig. 6 **a** Optical and **b** SEM micrographs showing the interface of 3Y-TZP/430L SS composite layer sintered in argon at 1,350 °C for 240 min. The heating rate was 5 K min^{-1}

limited reaction area (or interlayer diffusion zone) between the zirconia and stainless steel. Study the microstructure of vacuum sintered 3Y-TZP/430L SS composite layer indicated the formation of more diffusive reaction (diffusion) zone (Fig. 7). It appeared that the tendency of reaction at the ceramic/metal interface was higher under vacuum compared with that of argon. This reaction seems to be accompanied by the formation of voids at the diffusion boundary. Figure 8 shows the elemental distribution profile along the boundary of the composite layer sintered in vacuum. The diffusion boundary with a thickness of about 5 μm was noticed. It seems that diffusion of the elements across the interface happened, leading to formation of a solid solution by ion exchange and the formation of interface.

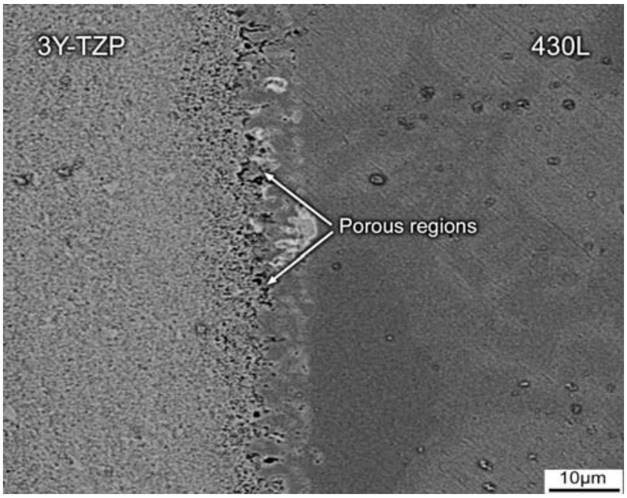

Fig. 7 SEM micrograph showing the interface zone of 3Y-TZP/430L SS sintered in vacuum at 1,350 °C for 240 min. The heating rate was 5 K min^{-1}

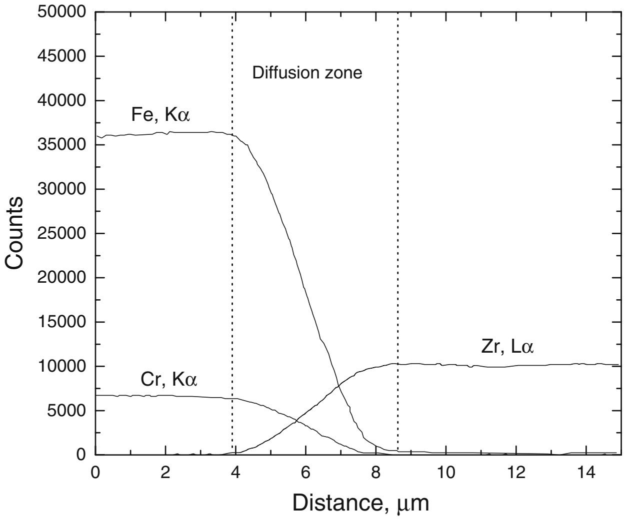

Fig. 8 EPMA line-scan profile showing the interlayer diffusion of the elements along the interface in 3Y-TZP/430L SS composite layer sintered at 1,350 °C in vacuum for 240 min

In light of the results presented so far, it became clear that sinter-joining of the zirconia ceramic to stainless steel is feasible but the mismatch shrinkage must be reduced or accommodated to prevent interface delamination and cracking. In the present work, elemental boron was added to the stainless steel powder with the aim of liquid phase formation upon sintering. It is supposed that the liquid phase ease materials transport during sintering and accommodate the relatively high mismatch strain; hence, it should facilitate the co-sintering and joining process. Figure 9 shows the variation of $\Delta\varepsilon$ and $\Delta\dot{\varepsilon}$ as a function of time for 3Y-TZP/430B composite layer during vacuum sintering. The nonisothermal and isothermal sintering steps are also indicated in the plot. As compared with the stainless steel powder without boron addition (Fig. 5), one can notice that the maximum mismatch strain increased. Nevertheless, microstructural study of samples (Fig. 10)

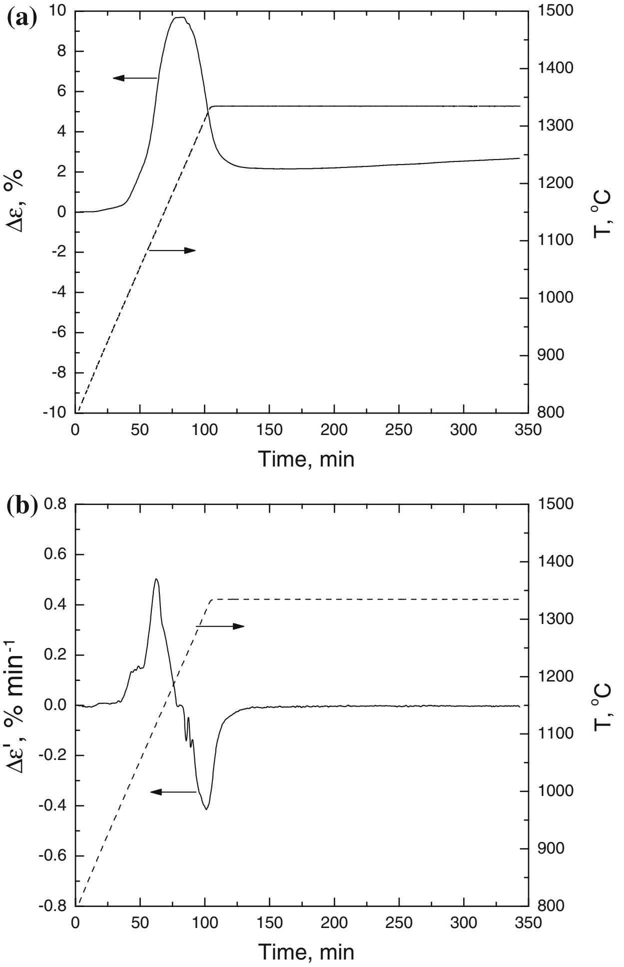

Fig. 9 Development of mismatch strain and mismatch strain rate during co-sintering of 3Y-TZP/430L SS composite layer with elemental boron addition as a function of time. The nonisothermal and isothermal sintering regions are indicated

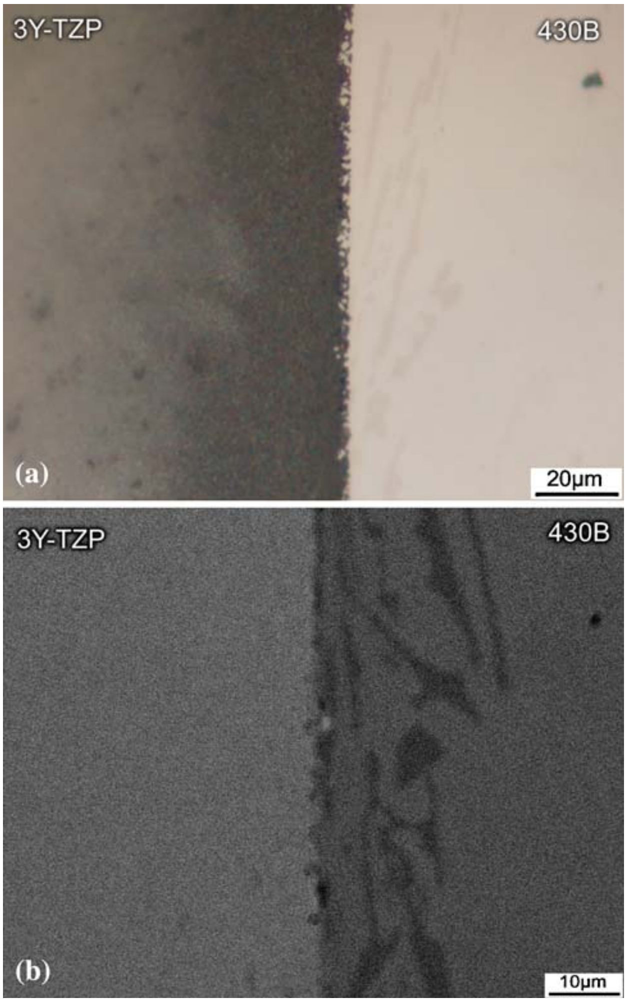

Fig. 10 **a** Optical and **b** SEM micrographs showing the interface of 3Y-TZP/430B SS composite layer sintered in argon at 1,350 °C for 240 min. The heating rate was 5 K min^{-1}

Table 4 Results of the shear-punch test performed on 3Y-TZP/430L and 3Y-TZP/430B composite layers sintered at 1,350 °C for 240 min

Composition	Shear strength [MPa]	
	Argon	Vacuum
3Y-TZP/430L	47 ± 5	66 ± 4
3Y-TZP/430B	91 ± 4	88 ± 3

indicated an improved interface formation during the sintering process in the presence of Fe–B melt. The crack-free interface is an indicator of stress accommodation by the liquid phase. The wider interface region of the composite layer (~5 μm) compared with that layer without B addition (<1 μm) also highlights the effect of liquid phase formation on the materials transport along the boundary.

The results of shear-punch tests performed on the sintered composite layers are reported in Table 4. The low bond strength of the 3Y-TZP/430L composite layer sintered in argon is noticeable. A higher strength was measured when vacuum sintering was afforded. Meanwhile, a significant enhancement in the bond strength was obtained when liquid phase sintering was performed. In this case, the effect of sintering atmosphere became marginal. In spite of higher mismatch strain during co-sintering of the boron added specimen (Fig. 9), the shear-punch results indicate the positive role of liquid phase sintering on the sinter-joining process. Here, it is worth noting that the relatively low strength of the joint-zone is partly linked to low density of zirconia ceramic (Table 3) and the voids presence in the boundary region (Fig. 7). A SEM micrograph taken from fractured surface of a sample sintered in vacuum is shown in Fig. 11. The fractured area shows the concern of porous area (signed B) created close to the joint boundary. A week or nonbonded area (signed A) is also visible.

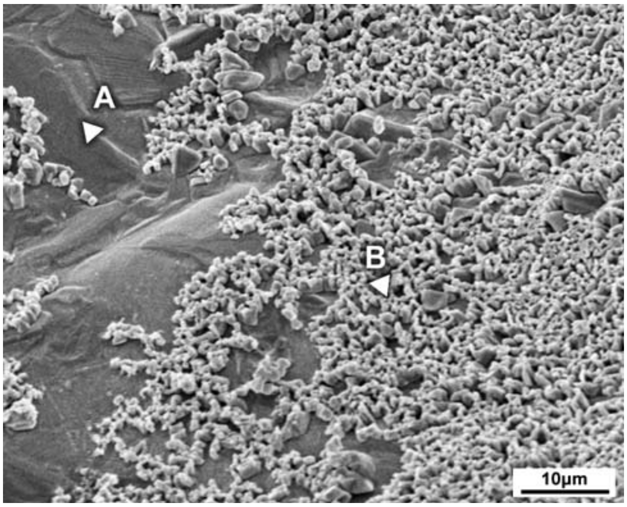

Fig. 11 SEM micrograph from fractured boundary of a vacuum sintered 3Y-TZP/430L SS joint; **a** weak or non-bonded areas and **b** porous structure in ceramic side close to the boundary

Discussion

It was shown that joining of zirconia ceramic to 430L stainless steel is feasible by the co-sintering process. It appeared that a metallurgical bond can be formed at the high temperature while the mismatch stresses at the interface are minimal. The origin for inducing mismatch stresses is two fold. First, different shrinkage rates upon sintering can lead to formation of biaxial stresses at the interface zone. Second, the difference between coefficient of thermal expansion (CTE) values of the two layers can induce interfacial stresses during cooling of the composite layer to the ambient temperature. Since the CTE values of 3Y-TZP (9.2×10^{-6}/°C) and 430L SS (10.1×10^{-6}/°C) are very close, the later should be minimized. To estimate the magnitude and distribution of residual stresses, finite-element analysis (FEM) was carried out with assumption of pure elastic behavior of the ceramic and elastic-pure plastic behavior of the metal layer. Here, a nonlinear total Lagrangian finite-element code with the ability of modeling thermomechanical constitutive equations was employed. Figure 12a shows the model containing 3- and 4-node axisymmetric elements, which are generated with the aid of advancing front meshing scheme. In the boundary region, smaller elements were used to improve the accuracy of calculation. The material assumed to be isotropic and the parameters used for simulation are listed in Table 5. The simulation was carried out for cooling rate of 10 K min^{-1} from 1,350 °C to ambient temperature in accordance with the experimental procedure. The residual radial stress developing at the central region of the 3Y-TZP/430L composite layer is shown in Fig. 12b. It appears that the maximum residual tensile stress is concentrated in the metal at the interface of the joint, and it transforms to compressive near the free surface. On the other side, the ceramic resists against a reverse stress distribution. The stress distribution ranges between −90 and 90 MPa, which is not very high to be severely dangerous for the joint endurance. It is worthy to mention that this stress level is remarkably lower than other investigated systems, for example −916 to 2,377 MPa for 4140/W/Si_3N_4 [61], −919 to 1,830 MPa for 4140/W/Nb/Si_3N_4 [61], and 364 MPa for V/Al_2O_3 [19], because the difference in the CTE values in the present work is relatively small.

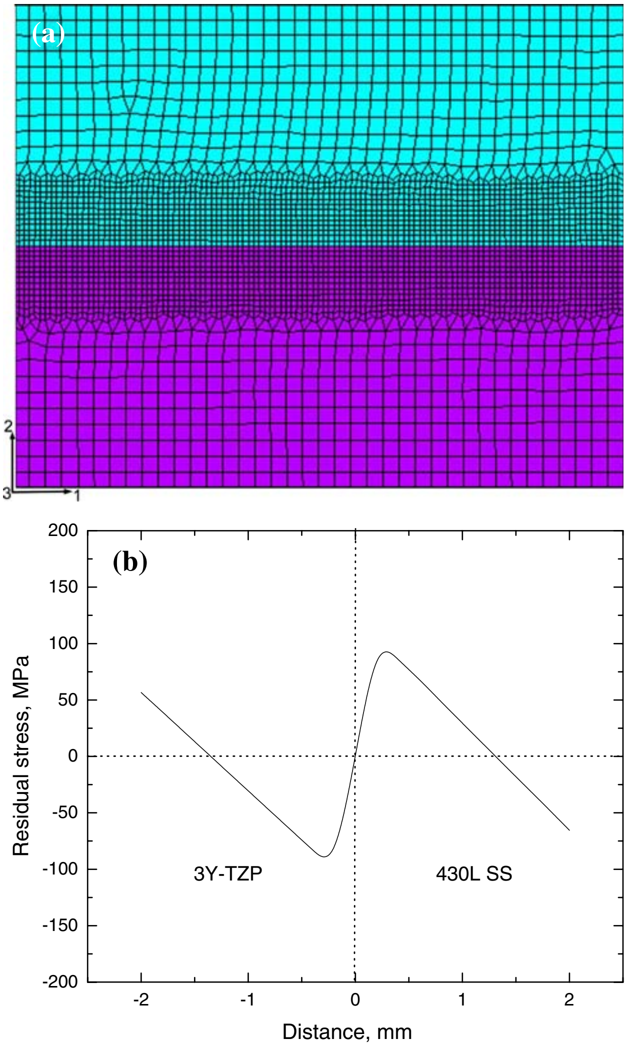

Fig. 12 **a** Axisymmetric model of the metal/ceramic joints with quadrilateral element and **b** residual radial stress (σ_1) along the axis of the 3Y-TZP/430L SS joint

The above analysis indicated that the key parameter for successful manufacturing is how to control the shrinkage rate during sintering and the total shrinkage after sintering. The powder characteristics (size, shape, etc.), the green density of the layers, and sintering condition (temperature, heating rate, atmosphere, etc.) determine the sintering

Table 5 Materials properties used for FEM analysis

Material	Poison ratio	Young modulus (GPa)	Thermal conductivity (W/m °C)	Specific heat capacity (J/kg °C)	Yield strength (MPa) at *T* (°C)					Coefficient of thermal expansion (10^{-6}/°C) at *T* (°C)				
					25	250	500	750	1000	25	250	500	750	1000
3Y-TZP	0.27	200	2.4	577	–	–	–	–	–	9.2	9.3	9.4	9.7	10.1
430 SS	0.28	210	23.9	460	310	213	174	103	65	10.1	10.6	11.2	11.5	11.9

mismatch shrinkage between the two components. Generally, 430L stainless steel exhibits faster sintering kinetics compared with that of zirconia due to the high diffusion rate in the ferritic phase as well as lower melting point of the steel. To increase the sintering compatibility, nanocrystalline 3Y-TZP powder was used in the present work in order to enhance the sintering rate. Dilatometric study [62] indicated that the temperature of sintering starts of nanocrystalline 3Y-TZP decreases about 180 °C compared with fine zirconia ceramic in an argon atmosphere. The temperature of maximum shrinkage rate is also reduced about 50 °C. Meanwhile the sintering kinetics of the zirconia ceramic is faster in argon than vacuum (Table 2). Experimental results (Fig. 5) indicated better sintering compatibility between the zirconia and stainless steel during vacuum sintering. The maximum mismatch strain and strain rate occurred at around 1,150 °C with the values of 7.5% and 0.2%/min, respectively. These values are 8.8% and 0.2%/min during sintering under argon. Microstructural study of the interface zone (Fig. 6) indicated the bond formation upon sintering in the argon atmosphere. The amount of the mismatch strain is high in both argon and vacuum sintering, which increases the propensity for fracture of the ceramic and is dangerous for the joint endurance. It is suggested that a part of mismatch strain could be accommodated by deformation of the steel layer at the high temperature. Sintering of 430L SS starts at 939 °C and proceeds with the highest rate at 1,024 °C in vacuum atmosphere (Table 2). Therefore, at around 1,150 °C, the stainless-steel layer is solid and soft to absorb some of the stresses by deformation. Meanwhile, the mismatch strain and strain rate between the zirconia ceramic and stainless steel during co-sintering are relatively high; almost a sound interface was observed (Fig. 7) at least in some areas. Park et al. [63] have shown that when the CTE mismatch of base materials is relatively small, the CTE of the interlayer is as important as its ductility in reducing the strain energy by inducing more plastic deformation in the interlayer. The analysis of the interface zone indicated a sharp boundary layer between the ceramic and stainless steel after argon sintering (Fig. 6) and more diffusive reaction zone after vacuum sintering (Fig. 7). It is well known that the oxygen ions have high conductivity in yitria stabilized zirconia [64]. It is suggestible that increasing of oxygen vacancies in zirconia under the vacuum atmosphere accelerated the diffusion rate [4] and assisted the probable reactions with stainless steel. Qin and Derby [65] have studied the reactions between NiCr alloy with zirconia under vacuum and found the formation of a reaction layer within the composition range of $NiO_{1-x}Cr_2O_{3-y}ZrO_{2-z}$ ($0 < x, \ y, \ z < 1$), which will be dissolved when the annealing is prolonged in vacuum. They have also shown the tendency of chromium to absorb the oxygen at the joint interface. Oxygen depletion of zirconia ceramics during vacuum sintering has been known for a long [4]. Durov et al. [66] have shown that nonstoichiometric zirconia is obtained after vacuum sintering. They have also reported the improved wetability of the nonstoichiometric zirconia due to the increase in oxygen vacancies. Therefore, during sintering of 3Y-TZP/430L composite layer, Cr should play a critical role on the formation of reaction interlayer, particularly under vacuum sintering. The formation of a reaction layer between zirconia ceramic and titanium [67] and Co–Cr–Mo alloy [15] using thermodynamics calculations and experimental evidences have been shown by other as well. Therefore, in addition to the lower amount of mismatch strain in the case of vacuum sintering, the formation of ∼5 μm reaction layer could accommodates some stresses leading to direct joining.

Similar discussion can be put forward when elemental boron was added to the stainless steel. As shown in Fig. 9, although B addition increased the amount of mismatch strain during the nonisothermal heating cycle, sinter-joining was attained (Fig. 10). Higher bond strength was also measured in the presence of boron (Table 4). It is suggested that the formation of Fe–B liquid phase at high temperature affects the wetting angle of ceramic [68–70]. Moreover, the melt formation enhances the diffusion rate of elements. Furthermore, the liquid phase penetrates to the micro-porosities and improves the joint strength by means of mechanical snags. In other words, improvement of the interface strength of the 3Y-TZP/430B composite can be attributed to the liquid phase spreading at the interface. Meanwhile the positive role of Cr on the formation of the reaction layer can be enhanced in the presence of B. Nakashima et al. [71] have reported segregation of Cr at the interface of copper melt/zirconia interface that improves joining. Therefore, in the presence of boron, the interface layer is enhanced that affects the accommodation of stresses at the bonding zone. It also contributes in an improvement in the joint strength.

Conclusion

The co-sintering of 3Y-TZP/430L stainless-steel composite layers was investigated. The following findings can be summarized.

- The sintering compatibility between the zirconia ceramic and stainless steel can be improved by using nanocrystalline 3Y-TZP.
- The sintering compatibility is higher in vacuum sintering (lower mismatch strain and strain rate) compared with argon atmosphere.
- Analysis of the stress distribution around the interface by FEM indicated that the maximum residual tensile stress is concentrated in the metal at the interface of the joint, and it transforms to compressive near the free surface. On the other side, the ceramic resists against a reverse stress distribution.
- Cr was found to play a key role on the joining of the zirconia ceramic to stainless steel.
- Formation of a reaction layer at the interface can accommodates some of the stresses at the interface region.
- The positive effect of elemental boron on the co-sintering of 3Y-TZP/430L SS was shown. Although the amount of sintering-shrinkage incompatibility increases, the formation of Fe–B melt contributes in the sinter-joining process by wetting the ceramic, enhancing the diffusion of Cr, decreasing the non-bonded areas, and penetrating to the pores and making mechanical snags.

References

1. Kim KT, Kim HG, Jang HM (1998) Int J Eng Sci 36:1295
2. Correia RN, Emiliano JV (1998) J Mater Sci 33:215. doi:10.1023/A:1004378520526
3. Mazaheri M, Simchi A, Golestani-Fard F (2008) J Eur Ceram Soc 28:2933
4. Munoz MC, Gallego S, Beltran JI, Cerda J (2006) Surf Sci Rep 61:303
5. Jadoon AK, Ralph B, Hornsby PR (2004) J Mater Proc Technol 152:257
6. Singh M, Shpargel TP, Asthana R (2008) J Mater Sci 43:23. doi:10.1007/s10853-007-1985-z
7. Akselsen OM (1992) J Mater Sci 27:1989. doi:10.1007/BF01117909
8. Wang Z, Qian J, Cao J, Wang S, Wen T (2007) J Alloys Compd 437:264
9. Harach DJ, Vecchio KS (2001) Met Mater Trans A 32:1493
10. Yeo JG, Jung YG, Choi SC (1998) J Eur Ceram Soc 18:1281
11. Biswas K, Upadhyaya GS (1998) Mater Des 19:231
12. Yun JW, Lombardo SJ (2008) J Am Ceram Soc 91:1553
13. Larker R, Wei LY, Loberg B, Olsson M, Johansson S (1994) J Mater Sci 29:4404. doi:10.1007/BF00414229
14. Zhang W, Xie J, Wang C (2004) Mater Sci Eng A 382:371
15. Yen SK, Guo MJ, Zan HZ (2001) Biomaterials 22:125
16. Hussain P, Isnin A (2001) J Mater Proc Technol 113:222
17. Scheu C, Gao M, Oh SH, Dehm G, Klein S, Tomsia AP, Rühle M (2006) J Mater Sci 41:5161. doi:10.1007/s10853-006-0073-0
18. Li J, Xiao P (2004) J Eur Ceram Soc 24:2149
19. Nemoto Y, Ueda K, Satou M, Hasegawa A, Katsunori K (1998) J Nucl Mater 258–263:1517
20. Vila M, Martinez ML, Prieto C, Miranzo P, Osendi MI, Terry A, Vaughan G (2004) Powder Technol 148:60
21. Yeo JG, Jung YG, Choi S-C (1998) Mater Lett 37:304
22. Ozawa M, Kawagoe M, Suzuku S (2004) J Mater Sci 39:1337. doi:10.1023/B:JMSC.0000013894.68512.a5
23. Li JQ, Zeng XR, Tang JN, Xiao P (2003) J Eur Ceram Soc 23:1847
24. Muller AC, Herbstritt D, Ivers-Tiffe E (2002) Solid State Ion 152–153:537
25. Li J, Xiao P (2001) J Mater Sci 36:1383. doi:10.1023/A:1017503503711
26. Morsi K, Patel VV, Moon KS, Garay JE (2008) J Mater Sci 43:4050. doi:10.1007/s10853-007-2225-2
27. Vanmeensel K, Huang SG, Laptev A, Salehi SA, Swarnakar AK, Biest OV, Vleugels J (2008) J Mater Sci 43:6435. doi:10.1007/s10853-008-2631-0
28. Lee JG, Ma HA, Lee XL, Zheng YJ, Zuo GH, Jia X (2007) J Mater Sci 42:9460. doi:10.1007/s10853-007-1934-x
29. Bruck HA, Shabana YM, Xu B, Laskis JP (2007) J Mater Sci 42:7708. doi:10.1007/s10853-007-1675-x
30. Kodera Y, Toyofuku N, Yamasaki H, Ohyanagi M, Munir ZA (2008) J Mater Sci 43:6422. doi:10.1007/s10853-008-2782-z
31. Muroi M, Trotter G, McCormick PG, Kawahara M, Tokita M (2008) J Mater Sci 43:6376. doi:10.1007/s10853-008-2559-4
32. MacAskill IA, Bishop DP (2007) J Mater Sci 42:4149. doi:10.1007/s10853-006-0893-y
33. Ruh A, Dieckmann AM, Heldele R, Piotter V, Ruprecht R, Munzinger C, Fleischer J, Haußelt J (2008) Microsyst Technol 14:1805. doi:10.1007/S00542-008-0646-8
34. Stephenson DJ (2000) Ann CIRP 49/1:191
35. Alcock JR, Logan PM, Stephenson DJ (1998) Surf Coat Technol 105:65
36. Heaney DF, Suri P, German RM (2003) J Mater Sci 38:4869. doi:10.1023/B:JMSC.0000004407.63082.f1
37. Imgrund P, Rota A, Simchi A (2008) J Mater Proc Technol 200:259
38. Imgrund P, Rota A, Petzoldt F, Simchi A (2007) Int J Adv Manuf Tech 33:176
39. Simchi A, Rota A, Imgrund P (2006) Mater Sci Eng A 424:282
40. Simchi A (2006) Met Mater Trans A 37:2549
41. Firozdour V, Simchi A, Kokabi AH (2007) J Mater Sci 43:55. doi:10.1007/s10853-007-2077-9
42. Dourandish M, Simchi A, Godlinski D (2008) Mater Sci Eng A 472:338
43. Feng J, Qiu M, Fan Y, Xu N (2007) J Membrane Sci 305:20
44. Baumann A, Moritz T, Lenk R (2007) Keram Z 59(5):346
45. Baumann AA, Moritz T, Lenk R (2007) Proceedings of European Powder Metallurgy Congress and Exhibition (EURO PM2007), vol 2. Toulouse, France, October 2007, p 189
46. Menon M, Chen IW (1999) J Am Ceram Soc 82:3422
47. Cai PZ, Green DJ, Messing GL (1997) J Am Ceram Soc 80:1929
48. Cai PZ, Green DJ, Messing GL (1997) J Am Ceram Soc 80:1940
49. Liao CH, Jean JH, Hung YY (2008) J Am Ceram Soc 91:648

50. Chang JC, Jean JH (2005) J Am Ceram Soc 88:1165
51. Boonyongmaneerat Y, Schuh CA (2006) Met Mater Trans 37A:1435
52. Delannay F, Pardoen D, Colin C (2005) Acta Mater 53:1655
53. Kazior J, Nykiel M, Pieczonka T, Marcu Puscas T, Molinari A (2004) J Mater Proc Technol 157–158:712
54. Özbek I, Konduk BA, Bindal C, Ucisik AH (2002) Vacuum 65:521
55. Tonnes C (1992) Met Powder Rep 47:49
56. Suri P, Heaney DF, German RM (2003) J Mater Sci 38:4875. doi:10.1023/B:JMSC.0000004408.44675.f6
57. Cullity BD (1978) Elements of X-ray diffraction, 2nd edn. Addison-Wesley Publishing Company Inc, Massachusetts
58. Theunissen GSAM, Winnubst AJA, Burggraaf AJ (1993) J Eur Ceram Soc 11:315
59. Sobczak N, Sobczak J, Nowak R, Kudyba A, Darlak P, Mikulowski B, Wojiechowski A (2005) J Mater Sci 40:2547. doi:10.1007/s10853-005-1990-z
60. Simchi A, Petzoldt F, Hartwig T (2005) Proceedings of Euro PM2005 Conference and Congress, vol 2. EPMA, Shrewsbury, UK, p 357
61. Sarkar K, Sund SE, Bose D, Yamanis J (1990) Math Comput Model 14:842
62. Mazaheri M (2007) MS Thesis. Sharif University of Technology, Tehran
63. Park JW, Mendez PF, Eagar TW (2005) Scr Mater 53:857
64. Darby RJ, Kumar RV (2008) J Mater Sci 43:6567. doi:10.1007/s10853-008-2983-5
65. Qin CD, Derby B (1993) J Mater Sci 28:4366. doi:10.1007/BF01154944
66. Durov AV, Naidich YV, Kostyuk BD (2005) J Mater Sci 40:2173. doi:10.1007/s10853-005-1928-5
67. Teng LD, Wang FM, Lia WC (2000) Mater Sci Eng A293:130
68. Ravi BG, Chaim R (2002) J Mater Sci 37:813. doi:10.1023/A:1013804301381
69. Nikolopoulos P, Ondracek G, Sotiropoulou D (1989) Ceram Int 15:201
70. Zhu J, Kamiya A, Yamada T, Shi W, Naganuma K, Mukai K (2002) Mat Sci Eng A327:117
71. Nakashima K, Matsumoto H, Mori K (2000) Acta Mater 48:4677